# Structure-Element Surface Modification Strategy Enhances the Antibacterial Performance of Zr-BMGs

Cezhi Du, Yuhe Yang, Lijuan Zheng, Tao Zhang, Xin Zhao,* and Chengyong Wang*

**Abstract**

Zirconium-based metallic glasses (Zr-BMGs) have attracted tremendous attention in healthcare fields, especially in the design of surgical tools and orthopedic implants, due to their unique amorphous structure; however, the application of Zr-BMG-based medical devices is hindered by bacterial contamination. Here, a structure-element strategy is proposed to improve the antibacterial performance of Zr-BMGs by surface laser nanostructuring and silver nanoparticle (AgNP) deposition. The laser nanostructuring process generates a disordered nanoparticle structure (NP) and laser-induced periodic surface structure (LIPSS) to decrease the surface bacterial adhesion and increase the internal antimicrobial ion release. Moreover, after Ag deposition and hydrogen peroxide (H2O2) treatment, the antibacterial adhesion ability of the Zr-BMG surface can be further improved without any influence on the crystallization of Zr-BMGs and the release of antibacterial copper/nickel (Cu/Ni). The antibacterial effect of the LIPSS and the NP surfaces presents over 90% bacterial killing ratio, which is superior to that of the naked Zr-BMGs with less than 60% bacterial killing ratio. In vitro and in vivo tests show that the Ag-deposited and H2O2-treated LIPSS surfaces exhibit an optimal balance between the antibacterial property and the biocompatibility compared with the polished, NP structured or LIPSS structured surfaces. It is assumed that such structure-element surface modification strategy can improve the antibacterial activity of metal-containing surgical tools and orthopedic implants, improving the success rate of medical treatment.

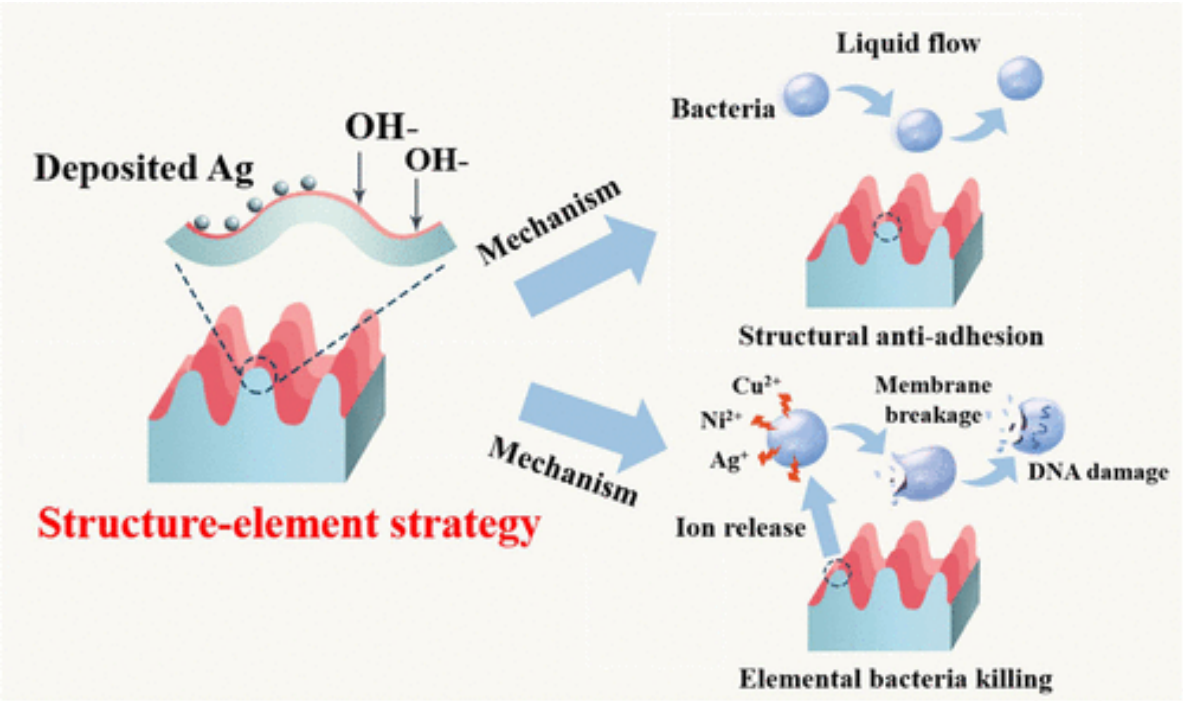

**KEYWORDS**: zirconium-based bulk metallic glass, laser nanostructuring, metal ion release, nanosilver deposition, antibacterial property

## Introduction

To reduce infection and improve the success rate of implantation, the development of antibacterial materials on the surface of medical devices is a hot spot in clinical research. Antibacterial surfaces can be obtained with antifouling strategy (antibacterial adhesion), bactericidal strategy (bacterial killing), or their combination. (1−4 )Bionic subbacterial nanostruc- tures mimicking the dragonfly wings, lotus leaf, and shark skin present inspiring antibacterial capacity because of the reduced contact area between the bacteria and the material surfaces. (5−8) Unfortunately, the infection may occur on these nano- structured surfaces due to the limited antibacterial efficiency. (9) Moreover, the high cost and time-consuming fabrication process (e.g., nanoimprint lithography or plasma etching) further impede their wide clinical application. (10−14) Recently, metal ions such as silver (Ag), copper (Cu), and nickel (Ni) ions have been applied to modify the medical implant surfaces to inhibit bacterial colonization. (15−17) These metal ions could kill bacteria by generating reactive oxygen species (ROS) through Fenton reactions or disrupting bacterial membranes by binding with the sulfhydryl groups of the bacterial membranes. (18,19) Meanwhile, the AgNO3 can be used to deposit Ag nanoparticles on the material surfaces. (20) However, a high concentration of antibacterial ions can also disrupt the cell membrane, resulting in detrimental cytotoxic effects. (21,22) That is, to improve the therapeutic efficacy of medical devices, antibacterial and biocompatible surfaces are highly desirable.

This study aimed to develop a synergic structure-element surface modification strategy to improve the antibacterial performance of medical implants while maintaining their biocompatibility. Zirconium (Zr)-based bulk metallic glasses (Zr-BMGs, e.g., Zr43.3Cu27.8Ni15.2Al9.1Ti4.6) were used as a model medical implant. These metallic glasses are popular in medical implants due to their high biocompatibility, high fracture toughness, and appropriate elastic modulus. Unfortunately, their clinical performance is often compromised due to bacterial infection (e.g., Staphylococcus aureus).23,24 To this end, the high-frequency laser direct writing technology was adopted to fabricate the laser-induced periodic surface structured (LIPSS) and disordered nanoparticle structured (NP) surfaces (Figure 1). Then, the nanosilver (Ag) deposition and hydrogen peroxide (H2O2) treatment were performed to further endow the Zr-BMGs with excellent antimicrobial effect. The resultant LIPSS and NP surfaces could effectively inhibit bacterial adhesion thanks to the reduced surface−bacteria contact area. These surfaces also exhibited increased Cu/Ni ion release due to the increased surface area and surface oxidation. The Ag deposition and H2O2 treatment could further enhance the antibacterial effect of the LIPSS and NP surfaces with over 90% bacterial killing ratio. Furthermore, the Ag-deposited and H2O2-treated LIPSS surfaces showed an optimum balance between the antibacterial properties and the cytocompatibility with over 90% cell viability and tissue compatibility. These findings collectively showed that our structure-element surface modification strategy could improve the antibacterial activity of medical devices with no detrimental effect on the surrounding cells/ tissues. As far as we know, this is the first study to integrate the structure-element modification in Zr-BMG surfaces to

enhance the antibacterial properties while maintaining biocompatibility. We assume that such laser surface processing and chemical modification strategy can achieve a highly effective anti- bacterial surface with superior biocompatibility and offers reference to the manufacturing of Zr-BMGs and other antibacterial medical devices.

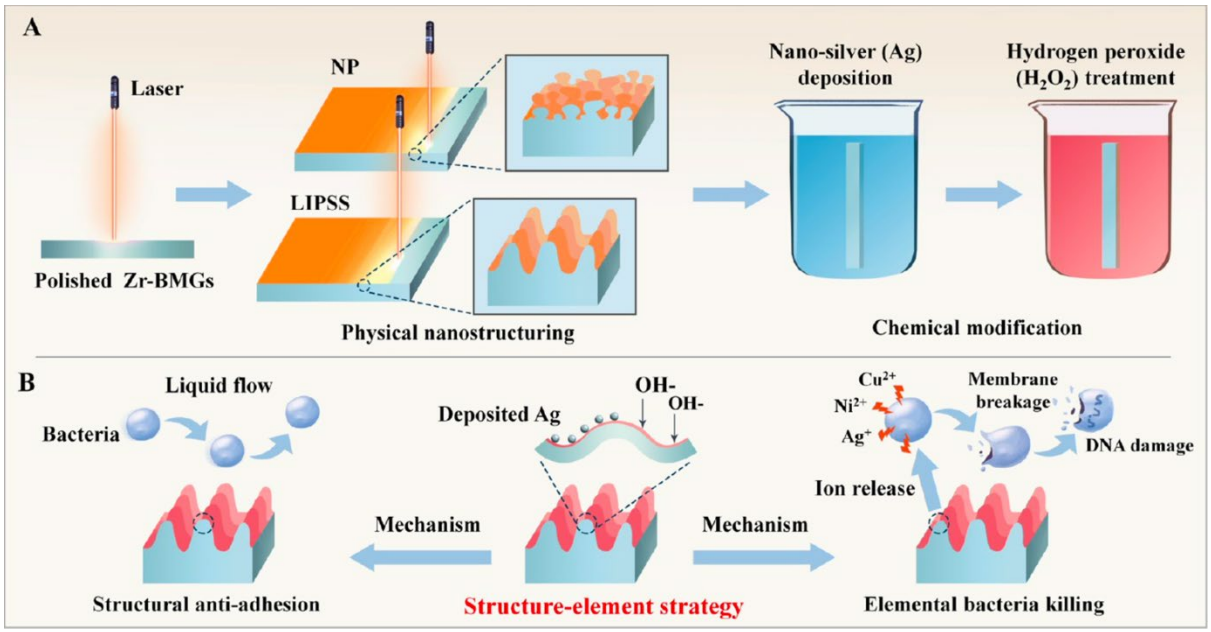


**Figure 1.** Schematic illustration of the fabrication and mechanism of antibacterial surfaces created using the structure-element strategy. (A) Fabrication process of the antibacterial surfaces with femtosecond laser irradiation followed by nanosilver (Ag) deposition and hydrogen peroxide (H2O2) treatment. (B) Antibacterial mechanism of the periodic nanostructured surfaces with Cu2+/Ni2+/Ag+ release potential created using the structure-element strategy.

## MATERIALS AND METHODS

**2.1. Materials.** Zr-BMG (Zr43.3Cu27.8Ni15.2Al9.1Ti4.6) specimens were prepared via a quick die casting process in vacuum to obtain their unique disordered atomic structure.25 The die casting size of the specimen was 10 × 10 × 1 mm3. Before laser processing, all samples were polished with 800, 1500, and 3000 grit sandpaper successively and then polished with a polyurethane pad and 10 000 grit sandpaper. The specimens were then cleaned in the ultrasonic bath for 20 min and dried in air.

**2.2. Surface Nanostructuring by Femtosecond Laser.** Femtosecond laser (Light Conversion Ltd., Lithuania) was used for the surface nanostructuring with a pulse width of 200 fs, central wavelength of 1030 nm, focus length of 160 mm, and laser beam size of 30 μm. The pulse energy was set at 3.5 μJ, with the ablation frequency at 100 kHz. The LIPSS structure was fabricated under 30 J/ cm2 energy intensity. The NP structure was manufactured as control with a scanning speed of 75 mm/s and energy intensity of 120 J/cm2. The interval between the scratching tracks was 10 μm for both surface nanostructures. All specimens were cleaned in the ultrasonic bath for 20 min and dried in air.

**2.3. Surface Chemical Modification.** To further enhance the bactericidal activity, chemical modification on the nanostructured Zr- BMG surface was performed with Ag deposition followed by H2O2 treatment. Briefly, a 1 mol/L silver nitrate (AgNO3) solution was used to deposit Ag on the nanostructured Zr-BMG surface at 80 °C for 1 h. Then, the Ag-deposited samples were cleaned with deionized water and further treated with 30% H2O2 solution for 2 h. The samples with either Ag deposition or H2O2 treatment were prepared as control. All samples were dried in air at 80 °C.

**2.4. Surface Characterization.** Scanning electron microscopy (SEM; Hitachi, Japan) and atomic force microscopy (AFM; Bruker) were used to examine the surface morphology. The surface area increase rate of the nanostructured surfaces was calculated using the equation

$$\gamma = \frac{A_{\ nanostuctured}}{A_{polished}}$$

where $A_{nanostructured}$ was the surface area of the nanostructured specimens and $A_{polished}$ was the surface area of the polished specimens based on the AFM measured topography. X-ray diffraction (XRD; Bruker) was used to examine the amorphous structure of the specimens. XRD analysis was performed using an X-ray diffractometer (Bruker, D8 ADVANCE) with a 2θ ranging from 10 to 90° at a step size of 0.01. The incident angle was 1°. Cu Kα radiation was used for the measurement. Moreover, an energy-dispersive spectrometer (EDS; Hitachi, Japan) was used to evaluate the surface element distribution. A goniometer (LAUDA Scientific Ltd., Germany) was used to examine the water contact angle of different surfaces. X-ray photoelectron spectroscopy (XPS; Thermo Fisher Scientific) was used to determine the valence state of Cu, Ni, and Ag of the treated samples. Inductively coupled plasma mass spectrometry (ICP-MS; Thermo Fisher Ltd.) was used to evaluate the ion release profile after the laser nanostructuring and chemical modification process. The ROS generation in phosphate-buffered saline (PBS) was additionally detected by the dichloro-dihydro-fluorescein diacetate (DCFH-DA) method. (26) To achieve adsorption−desorption equilibrium, Zr-BMG specimens were immersed in PBS for 24 h and subsequently incubated in 500 μL of diphenylisobenzofuran (DPBF) solution (10 mM; dissolved in DMSO) in dark for 5 min. The supernatant was then collected for ROS evaluation with ultraviolet−visible (UV) spectrometry. The water contact angle was measured based on the static sessile drop method using a contact angle goniometer (OSA- 200) with 5 μL of distilled water droplet. The diameter of the needle tip was 0.5 mm. The surface energy was measured based on Owens two-liquid method, and the deionized water and n-hexadecane were used to test the specimen surface contact angle. (27) The liquid parameters for surface energy measurement are shown in Table S1.

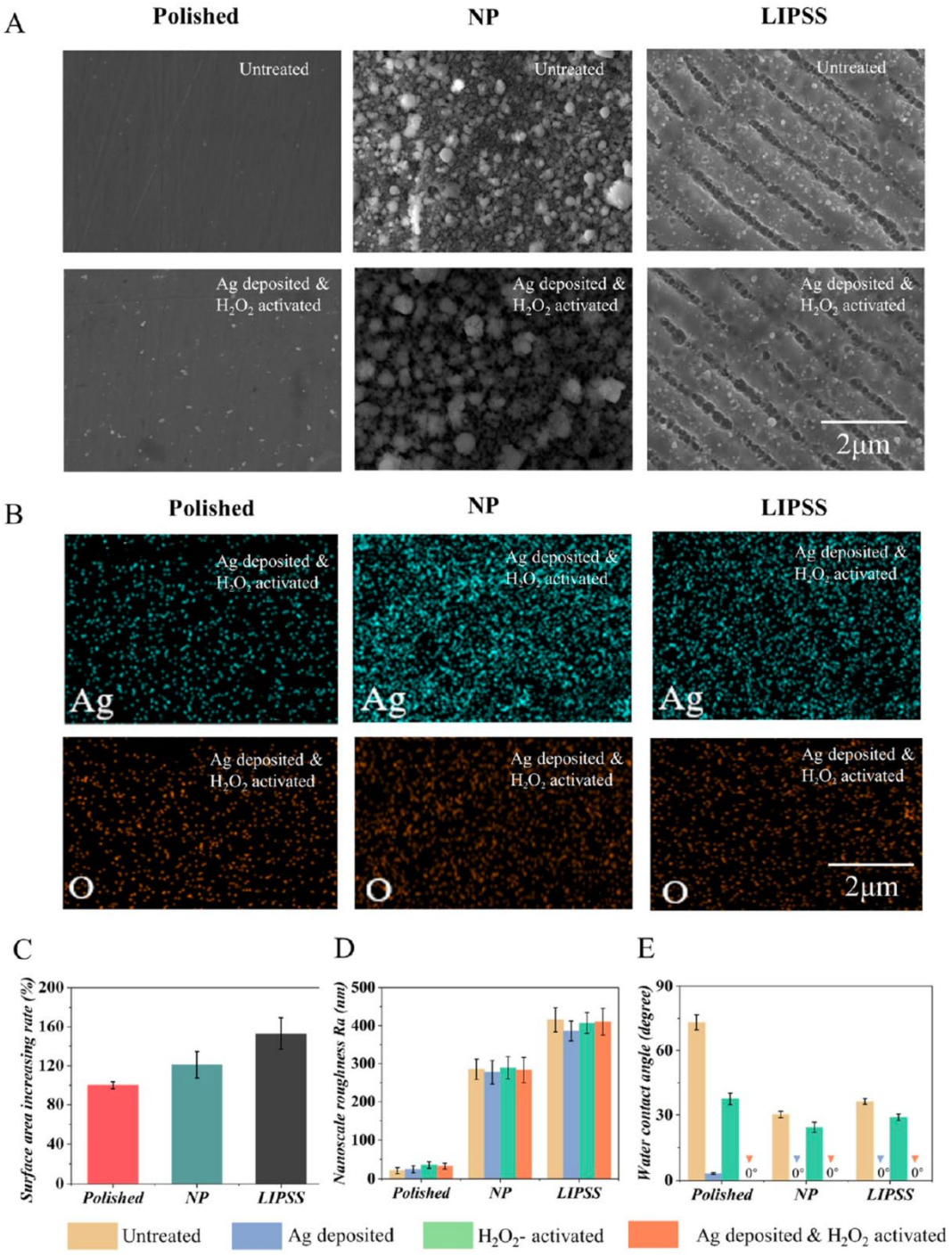


**Figure 2.** Surface characterizations of samples after laser nanostructuring and chemical modification. (A) Surface morphology evaluation of the polished, NP, and LIPSS surfaces with different surface treatments. (B) Surface Ag and oxygen distribution. (C) Specific surface area. (D) Surface nanoscale roughness and (E) surface energy evaluation of the polished, NP, and LIPSS surfaces with different treatments.

**2.5. Evaluation of Antibacterial Properties.** The antibacterial properties of the prepared specimens were evaluated by coincubating the specimens with 10 (7) CFU/mL *Staphylococcus aureu* (*S. aureus*, ATCC 6538). Briefly, after coincubation for 1, 7, and 14 days, the bacterial solutions were reincubated in agar plates for 24 h at 37 °C to evaluate the antibacterial properties. Bacterial inhibition ratio was calculated using the equation

$$Inhibition\ ratio\ (\%) = 100 - \frac{OD_{\ sample} - OD_{blank}}{OD_{control} - OD_{blank}} \times 100$$

where $OD_{sample}$, $OD_{control}$, and $OD_{blank}$ represent the OD values of the treated Zr-BMG group, untreated Zr-BMG group (negative control), and blank group (positive control, no specimen), respectively. The absorbance of the samples was measured at 600 nm wavelength using a spectrophotometer (Berthold, Germany). Fluorescence microscopy (Zeiss, Germany) was used to examine the surface coverage of the bacteria after staining with Alexa Fluor 488 Phalloidin (Thermo Fisher Scientific, China).

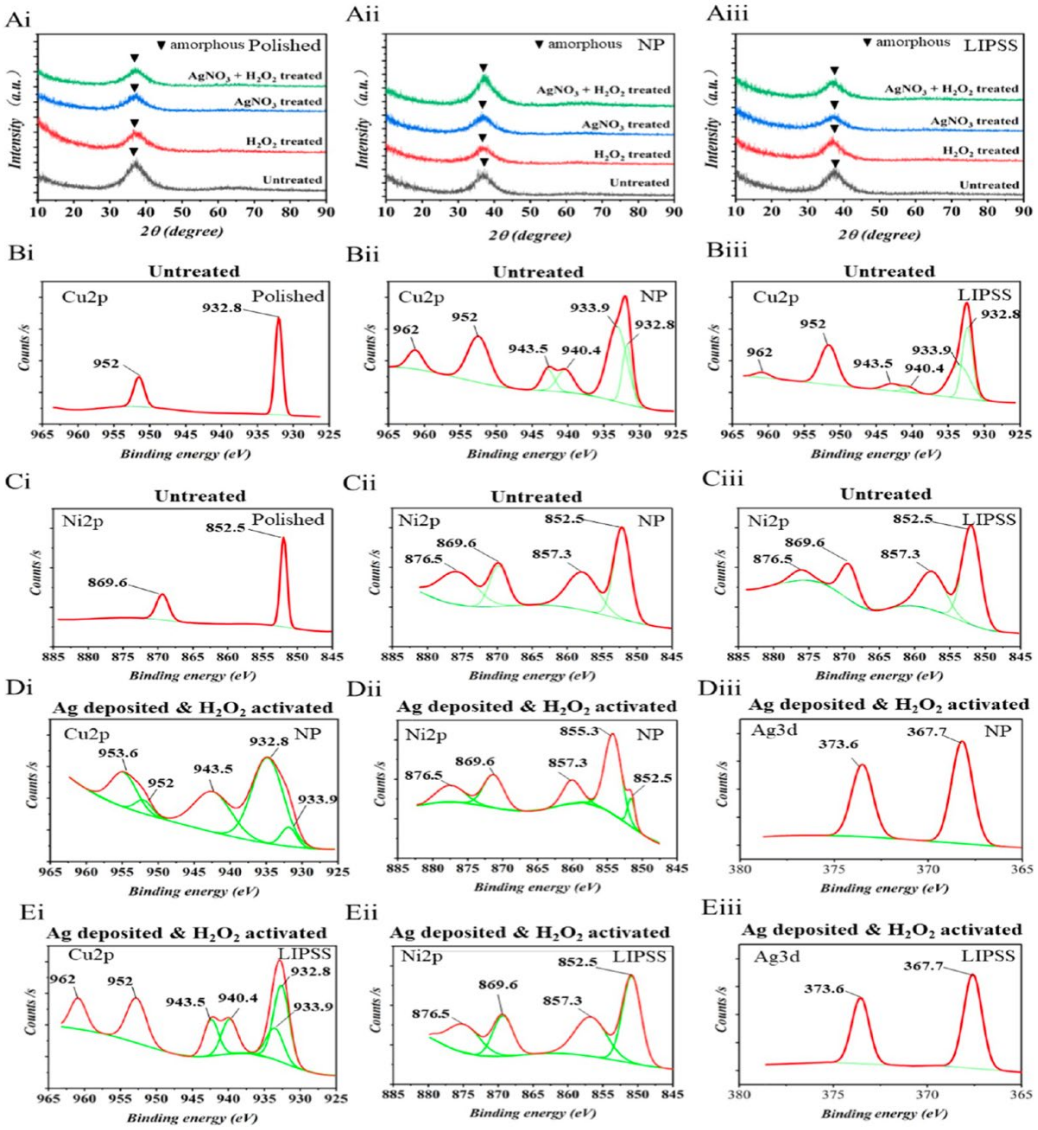


**Figure 3.** Surface amorphous status and antimicrobial element binding energy detection. (Ai) Polished surface, (Aii) NP surface, and (Aiii) LIPSS surface XRD peaks with 1° incident angle. Binding energy of Cu 2p at (Bi) polished, (Bii) NP, and (Biii) LIPSS surfaces without chemical treatment. Binding energy of Ni 2p at (Ci) polished, (Cii) NP, and (Ciii) LIPSS surfaces without chemical treatment. Binding energy of (Di) Cu 2p, (Dii) Ni 2p, and (Diii) Ag 3d at NP surfaces after nano-Ag deposition and H2O2 activation. Binding energy of (Ei) Cu 2p, (Eii) Ni 2p, and (Eiii) Ag 3d at LIPSS surfaces after nano-Ag deposition and H2O2 activation.

**2.6. Evaluation of the Bacteria Adhesion Force.** AFM was used to determine the adhesion force and contact morphology of the bacteria on the specimens in PBS. The polystyrene (PS) particle probe was developed by attaching a 5-μm diameter PS ball to a cantilever. The tip was subsequently immersed in an S. aureus solution ($10^7$ CFU/mL) for 10 min. The bacteria-coated PS particle probe was then immersed in PBS at 37 °C to measure the adhesion force. Force−distance curves were measured at 1 s contact time per point, and measurements were taken at 10 random points for each surface.

**2.7. Evaluation of In Vitro Cytocompatibility.** MC3T3-E1 cells (Guandao, China) were used to evaluate the cytocompatibility of the surface-modified specimens. All samples were cocultured with MC3T3-E1 cells at a density of $10^4$ cells/cm$^2$ at 37 °C with 5% $CO_2$. On day 1, 7, and 14, the cells were stained with Alexa Fluor 488 Phalloidin and DAPI (Thermo Fisher, China) to examine the cell growth behavior. May Grunwald and Giemsa (MGG) staining was used to evaluate the cell morphology after coculture with the specimens. The cell morphology after MGG staining was measured by an Olympus CX 46 microscope. Moreover, the cell counting kit-8 assay (CCK-8; Thermo Fisher, China) was used to evaluate the viability of MC3T3-E1 cells according to the previous protocol. (28) Cell viability was determined using the equation

$$Viability = \frac{(OD_{sample} - OD_{blank})}{(OD_{control} - OD_{blank})} \times 100\%$$

where $OD_{sample}$, $OD_{control}$, and $OD_{blank}$ represent the OD values for the laser nanostructured Zr-BMG group, polished Zr-BMG group (negative control), and blank group (positive control, no specimen), respectively.

**2.8. Evaluation of In Vivo Biocompatibility.** In vivo experi- ments were performed at the Guangdong Institute of Medical Instruments with approval. The antibacterial properties and in-tissue reaction of the samples were characterized by the bacterial infection implantation model, in which BALB/c mice (6 weeks, 30−35 g) were adopted. (29) Briefly, the specimens (10 × 1 × 1 mm3) were firstly cultured with S. aureus ($10^3$ CFU/mL) and washed with PBS. Then, a surgical operation was performed, in which the specimens were implanted and attached to the femur of BALB/c mice. After 14 days, the mice were euthanized and sacrificed. The implanted sections were collected for histological analysis using hematoxylin and eosin (H&E) staining. Mice blood was evaluated using a blood analyzer (IDEXX, Procyte DX) to characterize the inflammation response of the mice body. (30,31)

**2.9. Statistical Analysis.** All experiments were performed in triplicates unless otherwise stated. Statistical analysis was performed using SAS software (SAS). Means of the experimental data were compared using three-way tests, and differences were considered statistically significant at $p < 0.05$. Differences in bacterial adhesion rate means were analyzed by the least mean square method.

## 3. RESULTS AND DISCUSSION

**3.1. Surface Morphology and Property Character- ization.** Firstly, the morphology of the polished, NP, and LIPSS surfaces was examined by SEM. We found that the polished surfaces exhibited a smooth morphology without nanostructures due to the mechanical polishing process (Figure 2A). The NP surface was covered with disordered nanoparticles, whereas the LIPSS surface exhibited a periodic nanostructure with 800 nm width (Figure 2A). The cross- sectional topography evaluation of the NP structure and LIPSS structure was also conducted by SEM. It was found that there was no structural change in the subsurface layers after the high- energy nanostructuring process (Figure S1). Moreover, after surface chemical modification of Ag deposition and/or H2O2 treatment, the surface morphology of all groups remained unchanged, indicating that the chemical treatment would not affect the laser-induced nanostructures. To validate the Ag and oxygen element distributions on the treated surfaces, we performed the EDS analysis. We found that the Ag and oxygen elements were distributed evenly on all surfaces (Figure S1B). The Ag could bestow the surfaces with antibacterial property, and the oxygen could further enhance the surface bactericidal capacity. Moreover, the oxygen content of both laser nanostructured surfaces of the NP and the LIPSS significantly increased compared to those of the polished surfaces. Meanwhile, the $H_2O_2$ treatment could further increase the oxygen content in all groups, indicating increased surface oxidation status (Figure S3C). To evaluate the effect of laser nanostructuring on the surface area, the specific surface area analysis was performed. We found that the average area of the NP and LIPSS surfaces increased by approximately 21 and 52% compared to that of the polished surfaces (Figure 2C). The nanoscale roughness ($R_a$) evaluation also demonstrated that the LIPSS surface embodied the largest nanoscale waviness, with an $R_a$ of 457 ± 22 nm compared to that of the NP surfaces (285 ± 13 nm) or the polished surfaces (21 ± 8 nm) (Figure 2D). These findings implied that the LIPSS surfaces had better antibacterial adhesion capability than the NP or the polished surfaces due to the increased surface area and roughness and reduced contact area between the bacteria and the material surfaces.

In the liquid flow environment, the hydrophilic surfaces with nanostructures could decrease the bacterial retention due to the shear force generation. That is, surface hydrophilicity presents a critical effect on the antibacterial performance of the medical devices. (17) We thus performed the surface energy analysis of the samples to characterize the surface hydrophilicity. We found that the surface energy of the polished surfaces was approximately 27.4 mJ/m, which was smaller than the surface energy of all nanostructured specimens of the NP surfaces (39.3 mJ/m) and the LIPSS surfaces (35.5 mJ/m) (Figure 2E). This increased surface energy could improve the interaction between the surface and the water to increase the surface hydrophylicity. (27,32) The $H_2O_2$ treatment could also alter the surface hydrophilicity (Figure S3A). All of the $H_2O_2$- treated surfaces exhibited superior hydrophilicity, suggesting improved antibacterial adhesion property.

To further evaluate the effect of different treatment methods on the crystallization of Zr-BMG surfaces, we performed the XRD measurement and found that all Zr-BMG surfaces presented amorphous phase before and after laser nano- structuring, Ag deposition, and $H_2O_2$ treatment, indicating that both the laser nanostructuring and chemical treatment would not induce crystallization of Zr-BMGs (Figure 3A). In Zr-BMGs, the included elements (e.g., Cu, Ni) have been well recognized for their antibacterial potential, and the capacity could be affected by the valence state of the elements. Therefore, XPS analysis was used to evaluate the effect of the surface modification on the valence state of the antibacterial elements. The binding energy of Cu 2p3 (932.8 eV) on the polished surfaces implied that the Cu mainly occurred as $Cu^0$ (Figure 3B). On the contrary, the NP and LIPSS surfaces showed the presence of $Cu^{2+}$ with peaks at 933.9, 940.4, and 943.5 eV (Figure 3B). In addition, the peak intensity of Cu 2p3 on the NP surface was higher than that on the LIPSS surface, indicating the higher copper oxide content. In terms of the Ni element, the peak intensity of the Ni 2p spectrum at 852.5 eV on the polished surfaces indicated that $Ni^0$ was the most abundant element valence state. Interestingly, the binding energy of Ni 2p3 at 852.5 and 857.3 eV suggested that $Ni^0$ and $Ni^{2+}$ were the critical valence states on both the NP and LIPSS surfaces (Figure 3C). These valence-state shifts of Cu and Ni on the NP and LIPSS surfaces induced by laser nanostructuring may enhance the antibacterial activity of the elements. (31) To further validate if the chemical treatment could affect the valence state of the elements, we performed the XPS analysis of the $H_2O_2$-treated LIPSS surfaces. We found that the $H_2O_2$ treatment did not influence the valence state of Cu but could increase the $Ni^{2+}$ intensity, as indicated by the new peak at 855.3 eV (Figure 3D,E). Moreover, after Ag deposition and H2O2 treatment, the peak at 367.7 eV appeared, indicating the presence of $Ag^+$ (oxidized deposited nano-Ag particles) (Figure 3F).

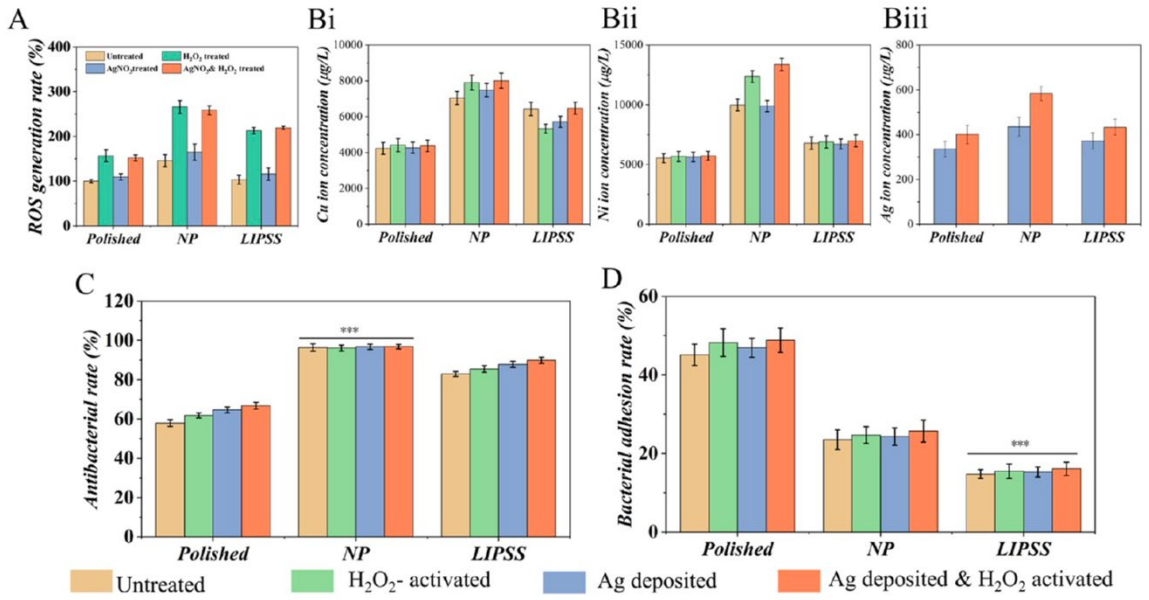


**Figure 4.** Evaluation of surface ROS generation, ion release, and antibacterial activity. (A) ROS production rate by samples immersed in PBS for 24 h. (Bi) Cu, (Bii) Ni, and (Biii) Ag ion concentration after immersion in PBS for 14 days. (C) Antibacterial activity of specimens after coculture with S. aureus for 14 days. (D) S. aureus adhesion ratio of specimens after coculture for 14 days (*$p < 0.05$).

**3.2. Antibacterial Element Release and Antibacterial Performance Evaluation.** As reported, oxidized surfaces could generate ROS to kill bacteria; (11) we therefore evaluated the ROS generation of different modified surfaces. We found that the Ag-deposited surfaces presented similar ROS generation compared to the untreated samples, indicating that Ag deposition did not induce the ROS generation. However, ROS generation on the $H_2O_2$-treated surfaces increased significantly compared to that on the polished surfaces or Ag-deposited surfaces (Figure 4A). We then evaluated the element release kinetics of Cu, Ni, and Ag of different samples for 1, 7, and 14 days, as these ions could affect the cytotoxicity of the implants. The Cu and Ni ion release was significantly increased from the NP surfaces compared to that from the polished surfaces or LIPSS surfaces (Figures 4B and S1). Moreover, the surface chemical treatment (e.g., Ag deposition and $H_2O_2$ treatment) presented little effect on the release of Cu and Ni ions. In terms of Ag ion release after chemical modification, we found that the NP surfaces presented significantly higher Ag release (Figure 4Biii). These findings showed that the laser nanostructuring process and Ag deposition and $H_2O_2$ treatment could substantially modulate the ROS generation and Cu/Ni/Ag ion release kinetics.

After evaluating the ion release, we proceeded to characterize the antibacterial performance of the specimens. The *S. aureus* was incubated with each specimen for 1, 7, and 14 days and subsequently reincubated in agar plates for 24 h to investigate the antibacterial activity. We found that numerous S. aureus colonies covered the reincubated agar plates in the polished group on day 1. In contrast, both the NP and LIPSS groups exhibited significantly decreased colony numbers, possibly attributed to the increased antibacterial ion release (Figure S4). The Ag deposition and $H_2O_2$ treatment could further enhance the antibacterial activity of all surfaces compared with the untreated specimens. Laser nanostructured surfaces subjected to Ag deposition and $H_2O_2$ treatment showed significantly higher S. aureus resistance after incubation for 7 and 14 days (Figures 4C and S8). The antibacterial activity of the NP surfaces was higher than 90% after incubation for 7 days. Although the antibacterial activity of LIPSS was lower than that of the NP surface, its antibacterial ratio was still over 90% after Ag deposition and $H_2O_2$ treatment, which was superior for the medical devices.

In addition to the surface chemical status, the bacterial adhesion behaviors could also influence the antibacterial activity of the prepared surfaces. The bacterial adhesion evaluation showed that the *S. aureus* adhesion ratio on the laser nanostructured surfaces was significantly lower than that on the polished surfaces (Figure 4D). After 90 min of direct contact with the bacteria, the LIPSS surfaces showed evident antifouling capacity (Figure S7). With the increasing bacteria contact time, the LIPSS surfaces maintained the lowest bacteria adhesion, suggesting its highest antibacterial adhesion activity. We then performed the bacterial adhesion force measurement using AFM to evaluate the bacterial adhesion behavior. The average adhesion force for the polished surfaces was approximately 5.7 and 2.4 nN for NP surfaces (Figure S5). The LIPSS surfaces demonstrated the lowest adhesion force of 1.8 nN, indicating its best antifouling performance.

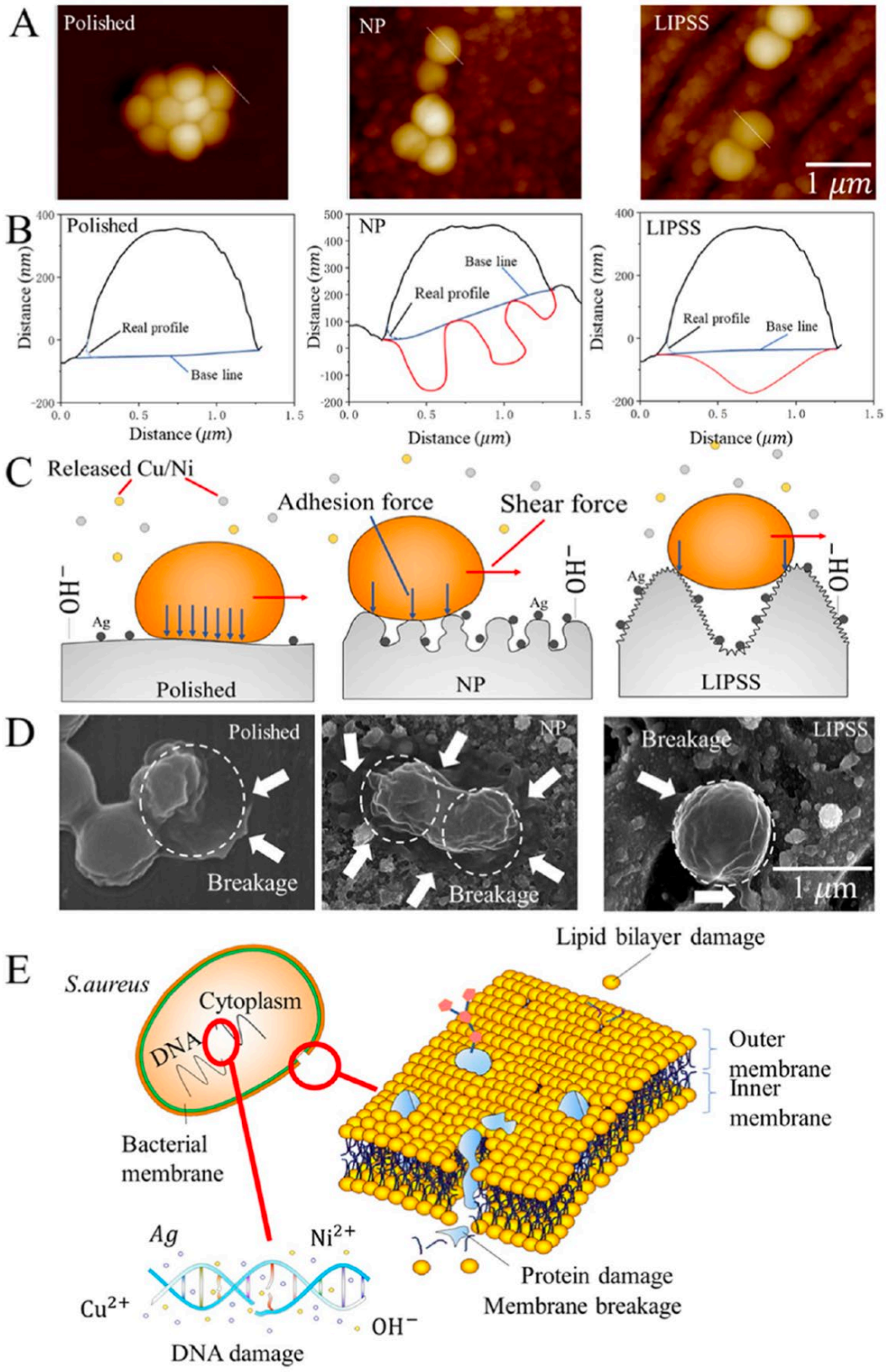


**Figure 5.** Antibacterial mechanism analysis. (A) S. aureus contact status and (B) cross-sectional evaluation of the polished, NP, and LIPSS surfaces in PBS. The white line indicates the data collection point. (C) Schematic diagram of bacterial adhesion behavior on different surfaces. (D) S. aureus membrane breakage on Ag-deposited and H2O2-treated surfaces. (E) Schematic diagram of the bactericidal mechanism.

**3.3. Antibacterial Mechanism Investigation.** In the liquid flow environment, the hydrophilic surfaces with nanostructures could decrease the bacterial retention due to the shear force generated by the cooperation of the could tightly adhere onto the polished surfaces with severe aggregation (Figure 5A). Intriguingly, bacteria on the NP and LIPSS surfaces presented distinctly separated morphologies without aggregation. The LIPSS surfaces exhibited the lowest adhesion force, which could be caused by the lowest adhesion area. (2,36,37) This decreased adhesion area was attributed to the large structural intervals of LIPSS, leading to the hill-top adhesion model, which could lift the bacteria to lower the contact area between the material surface and the bacteria (Figure 5B,C). (10,37)

Ag deposition efficiency on the nanostructured surfaces was higher than that on the polished surfaces. In addition, the nanostructured surfaces could promote the $H_2O_2$ treatment process to further increase the surface reactive oxygen species, which could enhance the bacterial inhibition. (38,39) Additionally, the NP surfaces had the highest Cu, Ni, and Ag release rates after Ag deposition and $H_2O_2$ treatment, exhibiting superior *S. aureus* elimination efficiency. Notably, the LIPSS surfaces exhibited similar antibacterial activity compared with the NP surfaces despite the slightly lower ion release rate. As reported, the released ions (e.g., $Ag^+$, $Cu^{2+}$, $Ni^{2+}$) could eliminate the bacteria through destruction of the bacterium membrane or destruction of the bacterium DNA. (22,40−42) The above results collectively demonstrated the synergic structure-element antibacterial mechanism of the NP and LIPSS surfaces.

The nanostructured surfaces could not only modulate the antibacterial performance but also regulate the antibacterial ion release owing to the increased surface area. We found that the Ag deposition efficiency on the nanostructured surfaces was higher than that on the polished surfaces. In addition, the nanostructured surfaces could promote the $H_2O_2$ treatment process to further increase the surface reactive oxygen species, which could enhance the bacterial inhibition. (38,39) Additionally, the NP surfaces had the highest Cu, Ni, and Ag release rates after Ag deposition and $H_2O_2$ treatment, exhibiting superior *S. aureus* elimination efficiency. Notably, the LIPSS surfaces exhibited similar antibacterial activity compared with the NP surfaces despite the slightly lower ion release rate. As reported, the released ions (e.g., $Ag^+$, $Cu^{2+}$, $Ni^{2+}$) could eliminate the bacteria through destruction of the bacterium membrane or destruction of the bacterium DNA. (22,40−42) The above results collectively demonstrated the synergic structure-element antibacterial mechanism of the NP and LIPSS surfaces.

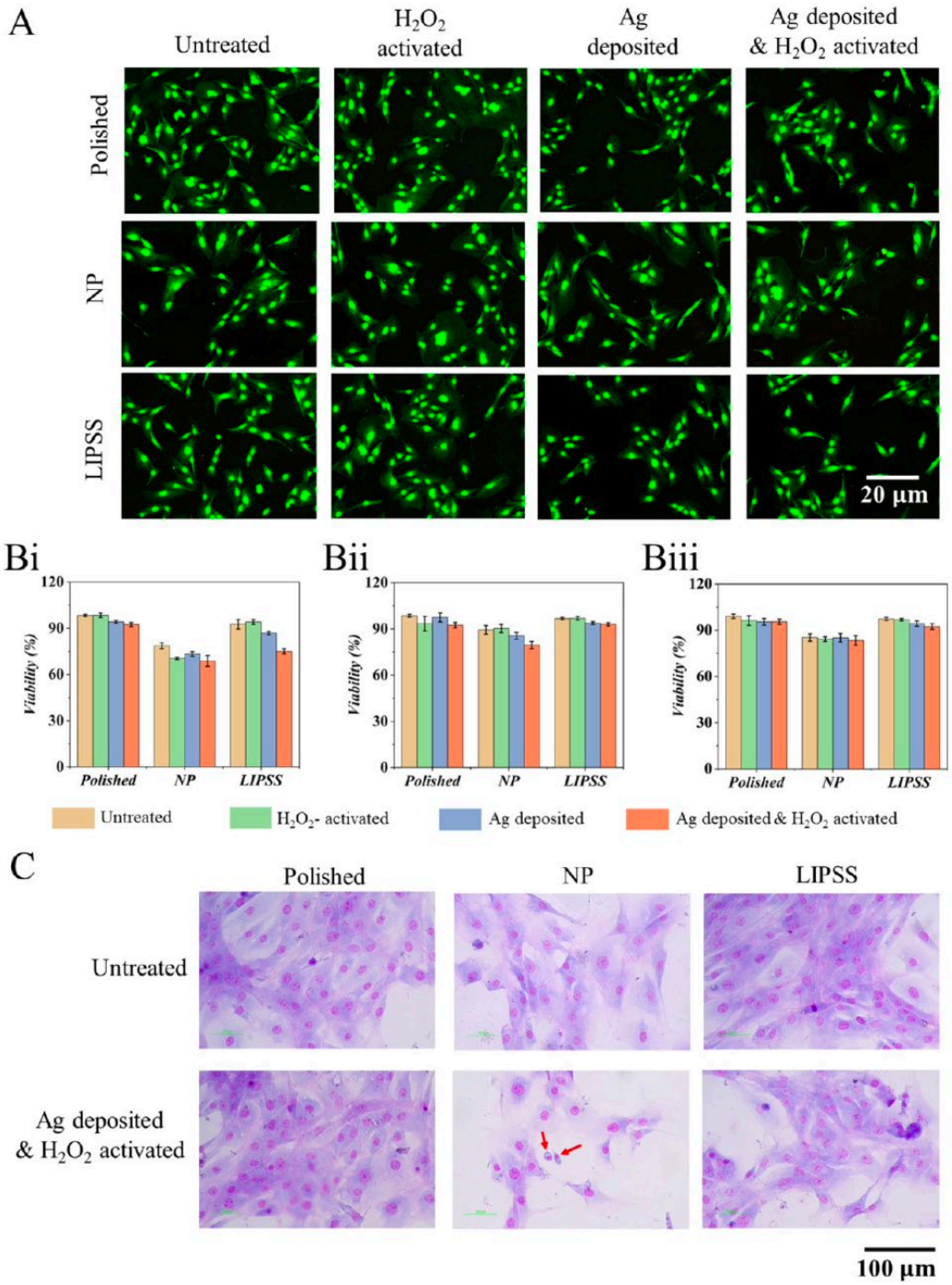


**Figure 6.** Evaluation of in vitro cytocompatibility of different samples. (A) MC3T3-E1 cell viability analysis of samples cocultured with the polished, NP, and LIPSS surfaces after incubation for 14 days. MC3T3-E1 cell viability after 1 (Bi), 7 (Bii), and 14 (Biii) days of coculture with the polished, NP, and LIPSS surfaces. (C) MC3T3-E1 cell morphology after 14 days of coculture with the untreated and Ag-deposited and H2O2- activated specimens stained with the MGG method.

**3.4. In Vitro Cytocompatibility.** Although the NP and LIPSS surfaces presented excellent antibacterial performance, the high release concentration of antibacterial ions (e.g., Ni ions) may induce cytotoxicity. (22,41) Therefore, MC3T3-E1 cells (a model cell line) were used to evaluate the cytocompatibility of the prepared surfaces. We cultured the MC3T3-E1 cells with different specimens for 1, 7, and 14 days. We

found that the cells in all groups presented normal morphology without any significant changes after day 14 (Figure 6A). CCK-8 assay was used to evaluate the cell viability of each group. The polished surface groups exhibited over 90% cell viability during the whole incubation time (Figure 6B). The LIPSS surface group showed a slightly lower cell viability compared to that of the polished surface group (~80%). However, the NP surface group showed the lowest cell viability (~70%). To detect the effect of the released ions on the cell membrane, we performed MGG staining to characterize the cell cytoplasm and nucleus. We found that the cells cultured with Ag-deposited and H2O2- activated NP specimens did not spread on the culture dish, as indicated by the red arrows in Figure 6C, which may be induced by the over-release of Ni ions. However, the Ni ion release did not change the cell membrane status in other groups (Figure 6C). The results demonstrated that the high concentration of Cu/Ni ion release from the NP group could impair the cell viability; however, the LIPSS surfaces with decreased Cu/Ni ion release presented an optimal balance between the cytotoxicity and the antibacterial performance.

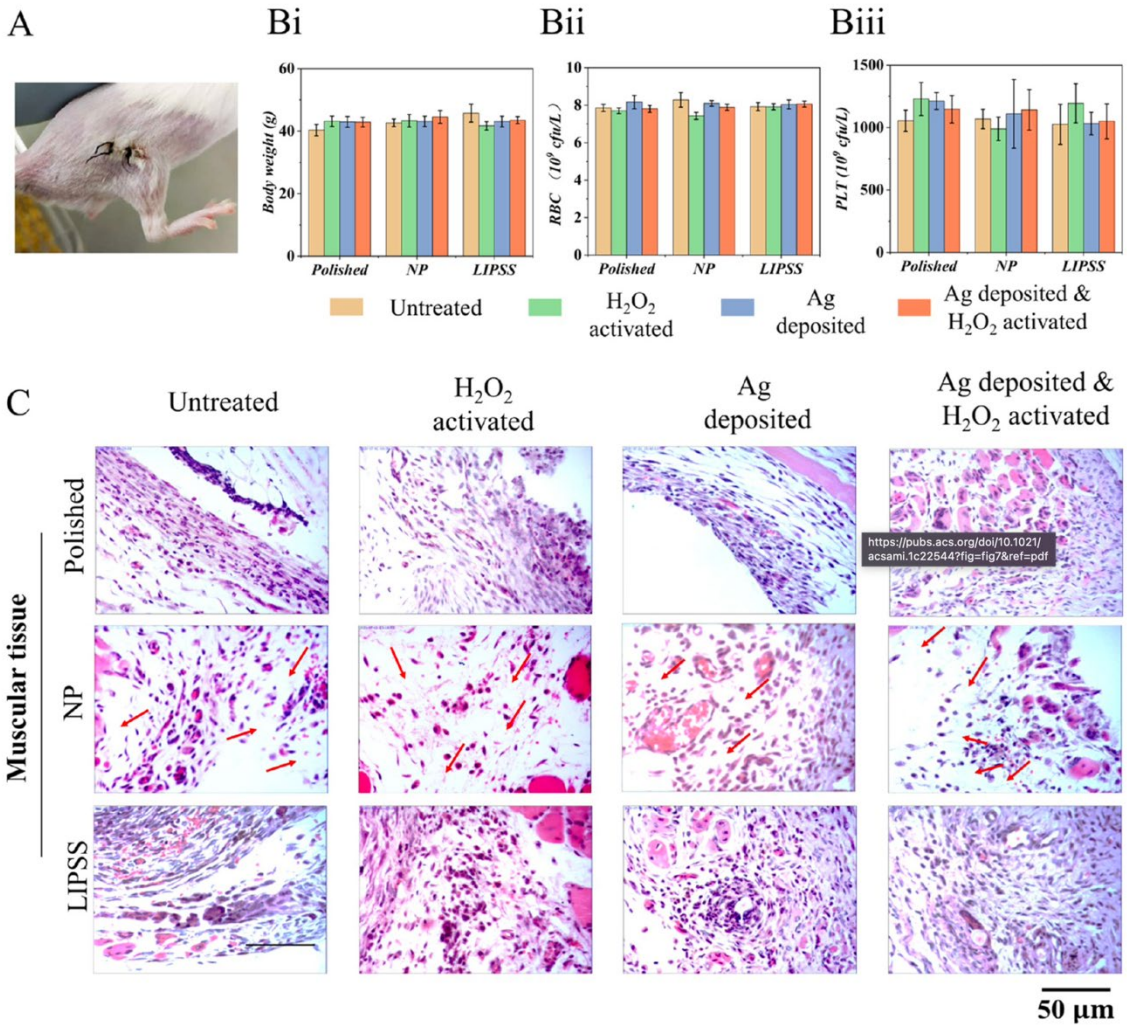


**Figure 7.** In vivo biocompatibility analyses of the treated and untreated Zr-BMGs. (A) Mice after implant surgery. (Bi) Body weight, (Bii) red blood cell counts, and (Biii) platelet densities at 14 days after implantation. (C) Muscular tissue histology analysis of the implanted area. Red arrows indicate fibrotic cells.

**3.5. In Vivo Biocompatibility Evaluation.** Although the above results proved the promising efficacy of our developed LIPSS surfaces with the balance of antibacterial and cytocompatibility properties, their clinical manifestation remained to be unexplored. We further evaluated the muscular and osseous tissue reactions of the processed Zr-BMGs (Figure 7A). Before implantation, all samples were immersed in the bacterial solution for 24 h. After 14 days, all mice were weighed between 38 and 43 g with no significant difference among the groups, indicating that the implantation process did not affect the mice growth (Figure 7B). Moreover, the red blood cell (RBC) and platelet (PLT) densities of the mice blood before and after implantation were within the normal range, with no significant difference between the treated Zr-BMG groups and the untreated Zr-BMG group (control) (Figures 7C and S9), indicating the antibacterial activity of the treated Zr-BMGs. Additionally, all mice did not exhibit marked inflammatory responses. Then, histology analysis was performed to investigate the in vivo biocompatibility of the specimens, in which the muscular and osseous tissues of the polished and LIPSS surface groups were shown to be slightly stimulated. In contrast, the muscular tissues in the NP surface group were significantly stimulated after implantation in the presence of inflammatory fibrotic cells, possibly due to the high Cu, Ni, and Ag ion release concentrations (Figures 7C and S4). Altogether, the LIPSS surface treated by Ag deposition and $H_2O_2$ exhibited an optimal balance between the antibacterial performance and the in vitro and in vivo biocompatibility.

## Conclusion

In conclusion, we developed a synergic structure-element surface modification strategy to improve the antibacterial properties of medical implants while maintaining the biocompatibility. Specifically, femtosecond laser surface structuring-processed surfaces are fabricated, and then Ag deposition and $H_2O_2$ treatment are conducted to endow the Zr-BMGs with balanced antibacterial performance and in vitro and in vivo biocompatibility. This balance is achieved due to the reduced material surface−bacteria contact area, increased hydrophilicity, and enhanced Cu/Ni/Ag ion release. It is assumed that such laser surface processing and chemical modification strategy can achieve a highly effective anti- bacterial surface with superior biocompatibility and offers reference to the manufacturing of Zr-BMG products (e.g., scalpels, bone plates, and vascular clamps) and other antibacterial medical devices.


## Acknowledgments

This work was supported by grants from the Guangdong Major Project of Basic and Applied Basic Research, China (No. 2019B030302010) and the National Natural Science Foundation of China (No. 51735003), the General Research Fund from the Research Grants Council of the Hong Kong Special Administrative Region, China (Project No. 15202119), and the intra-faculty fund (1-ZVPC) from the Hong Kong Polytechnic University.

## Reference


(1) Cloutier, M.; Mantovani, D.; Rosei, F. Antibacterial Coatings: Challenges, Perspectives, and Opportunities. Trends Biotechnol. 2015, 33, 637−652.
(2) Hasan, J.; Crawford, R. J.; Ivanova, E. P. Antibacterial Surfaces: The Quest for a new Generation of Biomaterials. Trends Biotechnol. 2013, 31, 295−304.
(3) Liu, Y.; Padmanabhan, J.; Cheung, B.; Liu, J.; Chen, Z.; Scanley, B. E.; Wesolowski, D.; Pressley, M.; Broadbridge, C. C.; Altman, S.; Schwarz, U. D.; Kyriakides, T. R.; Schroers, J. Combinatorial Development of Antibacterial Zr-Cu-Al-Ag Thin Film Metallic Glasses. Sci. Rep. 2016, 6, No. 26950.
(4) Sharifikolouei, E.; Najmi, Z.; Cochis, A.; Scalia, A. C.; Aliabadi, M.; Perero, S.; Rimondini, L. Generation of Cytocompatible Superhydrophobic Zr-Cu-Ag Metallic Glass Coatings with Antifouling Properties for Medical Textiles. Mater. Today Bio 2021, 12, No. 100148.
(5) Li, J.; Wang, G.; Meng, Q.; Ding, C.; Jiang, H.; Fang, Y. A Biomimetic Nano Hybrid Coating Based on the Lotus Effect and its Anti-Biofouling Behaviors. Appl. Surf. Sci. 2014, 315, 407−414.
(6) Jiang, R.; Hao, L.; Song, L.; Tian, L.; Fan, Y.; Zhao, J.; Liu, C.; Ming, W.; Ren, L. Lotus-Leaf-Inspired Hierarchical Structured Surface with Non-Fouling and Mechanical Bactericidal Performances. Chem. Eng. J. 2020, 398, No. 125609.
(7) Anselme, K.; Davidson, P.; Popa, A. M.; Giazzon, M.; Liley, M.; Ploux, L. The Interaction of Cells and Bacteria with Surfaces Structured at the Nanometre Scale. Acta Biomater. 2010, 6, 3824− 3846.
(8) Elbourne, A.; Crawford, R. J.; Ivanova, E. P. Nano-Structured Antimicrobial Surfaces: From Nature to Synthetic Analogues. J. Colloid Interface Sci. 2017, 508, 603−616.
(9) Yuan, Z.; He, Y.; Lin, C.; Liu, P.; Cai, K. Antibacterial Surface Design of Biomedical Titanium Materials for Orthopedic Applica- tions. J. Mater. Sci. Technol. 2021, 78, 51−67.
(10) Luan, Y.; Liu, S.; Pihl, M.; van der Mei, H. C.; Liu, J.; Hizal, F.; Choi, C.-H.; Chen, H.; Ren, Y.; Busscher, H. J. Bacterial Interactions with Nanostructured Surfaces. Curr. Opin. Colloid Interface Sci. 2018, 38, 170−189.
(11) Courvoisier, F.; Stoian, R.; Couairon, A. Ultrafast Laser Micro- and Nano-processing with Nondiffracting and Curved Beams. Opt. Laser Technol. 2016, 80, 125−137.
(12) Vadillo-Rodríguez, V.; Guerra-Garcia-Mora, A. I.; Perera-Costa, D.; Gonzalez-Martin, M. L.; Fernandez-Calderon, M. C. Bacterial Response to Spatially Organized Microtopographic Surface Patterns with Nanometer Scale Roughness. Colloids Surf., B 2018, 169, 340− 347.
(13) Hirano, M.; Hashimoto, M.; Miura, K.; Ohtsu, N. Fabrication of Antibacterial Nanopillar Surface on AISI 316 Stainless Steel through Argon Plasma Etching with Direct Current Discharge. Surf. Coat. Technol. 2021, 406, No. 126680.
(14) Dundar Arisoy, F.; Kolewe, K. W.; Homyak, B.; Kurtz, I. S.; Schiffman, J. D.; Watkins, J. J. Bioinspired Photocatalytic Shark-Skin Surfaces with Antibacterial and Antifouling Activity via Nanoimprint Lithography. ACS Appl. Mater. Interfaces 2018, 10, 20055−20063.
(15) Liu, W.; Li, J.; Cheng, M.; Wang, Q.; Qian, Y.; Yeung, K. W. K.; Chu, P. K.; Zhang, X. A Surface-Engineered Polyetheretherketone Biomaterial Implant with Direct and Immunoregulatory Antibacterial Activity Against Methicillin-Resistant Staphylococcus aureus. Biomate- rials 2019, 208, 8−20.
(16) Wang, X.; Li, R.; Liu, A.; Yue, C.; Wang, S.; Cheng, J.; Li, J.; Liu, Z. Syntheses, Crystal Structures, Antibacterial Activities of Cu(II) and Ni(II) Complexes based on Terpyridine Polycarboxylic Acid Ligand. J. Mol. Struct. 2019, 1184, 503−511.
(17) Chen, Y.; Ding, Y.; Zheng, J. A Polymer Nanocomposite Coating with Enhanced Hydrophilicity, Antibacterial and Antibiofoul- ing Properties: Role of Polymerizable Emulsifier/Anionic Ligand. Chem. Eng. J. 2020, 379, No. 122268.
(18) Zhang, Z.; He, X.; Zhou, C.; Reaume, M.; Wu, M.; Liu, B.; Lee, B. P. Iron Magnetic Nanoparticle-Induced ROS Generation from Catechol-Containing Microgel for Environmental and Biomedical Applications. ACS Appl. Mater. Interfaces 2020, 12, 21210−21220.
(19) Yang, B.; Ding, L.; Yao, H.; Chen, Y.; Shi, J. A Metal-Organic Framework (MOF) Fenton Nanoagent-Enabled Nanocatalytic Cancer Therapy in Synergy with Autophagy Inhibition. Adv. Mater. 2020, 32, No. 1907152.
(20) Ivanova, A. A.; Surmenev, R. A.; Surmeneva, M. A.; Mukhametkaliyev, T.; Loza, K.; Prymak, O.; Epple, M. Hybrid Biocomposite with a Tunable Anti-bacterial Activity and Bioactivity based on RF Magnetron Sputter Deposited Coating and Silver Nanoparticles. Appl. Surf. Sci. 2015, 329, 212−218.
(21) Bertero, E.; Hasegawa, M.; Staubli, S.; Pellicer, E.; Herrmann, I. K.; Sort, J.; Michler, J.; Philippe, L. Electrodeposition of Amorphous Fe-Cr-Ni Stainless Steel Alloy with High Corrosion Resistance, Low Cytotoxicity and Soft Magnetic Properties. Surf. Coat. Technol. 2018, 349, 745−751.
(22) Poornavaishnavi, C.; Gowthami, R.; Srikanth, K.; Bramhachari, P. V.; Venkatramaiah, N. Nickel Nanoparticles Induces Cytotoxicity, Cell Morphology and Oxidative Stress in Bluegill Sunfish (BF-2) Cells. Appl. Surf. Sci. 2019, 483, 1174−1181.

(23) Zimmerli, W. Clinical Presentation and Treatment of Orthopaedic Implant-associated Infection. J. Intern. Med. 2014, 276, 111−119.
(24) Arciola, C. R.; Alvi, F. I.; An, Y. H.; Campoccia, D.; Montanaro, L. Implant Infection and Infection Resistant Materials: A Mini Review. Int. J. Artif. Organs 2005, 28, 1119−1125.
(25) Zhang, T.; Meng, X.; Wang, C.; Li, L.; Yang, J.; Li, W.; Li, R.; Zhang, Y. Investigations of New Bulk Metallic Glass Alloys Fabricated using a High-Pressure Die-casting Method based on Industrial Grade Zr Raw Material. J. Alloys Compd. 2019, 792, 851−859.
(26) Yu, D.; Zha, Y.; Zhong, Z.; Ruan, Y.; Li, Z.; Sun, L.; Hou, S. Improved Detection of Reactive Oxygen Species by DCFH-DA: New Insight into Self-Amplification of Fluorescence Signal by Light Irradiation. Sens. Actuators, B 2021, 339, No. 129878.
(27) Mei, S.; Yang, L.; Pan, Y.; Wang, D.; Wang, X.; Tang, T.; Wei, J. Influences of Tantalum Pentoxide and Surface Coarsening on Surface Roughness, Hydrophilicity, Surface Energy, Protein Adsorption and Cell Responses to PEEK based Biocomposite. Colloids Surf., B 2019, 174, 207−215.
(28) Li, X. Q.; Yue, C. W.; Xu, W. H.; Lu, Y. H.; Huang, Y. J.; Tian, P.; Liu, T. A Milbemycin Compound Isolated from Streptomyces Sp. FJS31-2 with Cytotoxicity and Reversal of Cisplatin Resistance Activity in A549/DDP Cells. Biomed. Pharmacother. 2020, 128, No. 110322.
(29) Sun, Y.; Zhao, Y. Q.; Zeng, Q.; Wu, Y. W.; Hu, Y.; Duan, S.; Tang, Z.; Xu, F. J. Dual-Functional Implants with Antibacterial and Osteointegration-Promoting Performances. ACS Appl. Mater. Inter- faces 2019, 11, 36449−36457.
(30) Steven, S.; Dib, M.; Roohani, S.; Kashani, F.; Munzel, T.; Daiber, A. Time Response of Oxidative/Nitrosative Stress and Inflammation in LPS-Induced Endotoxaemia-A Comparative Study of Mice and Rats. Int. Mol. Sci. 2017, 18, 2176.
(31) Charrin, E.; Dube, J. J.; Connes, P.; Pialoux, V.; Ghosh, S.; Faes, C.; Ofori-Acquah, S. F.; Martin, C. Moderate Exercise Training Decreases Inflammation in Transgenic Sickle Cell Mice. Blood Cells, Mol., Dis. 2018, 69, 45−52.
(32) Çıtak, A.; Yarbas¸, T. Using Contact Angle Measurement Technique for Determination of the Surface Free Energy of B-SBA- 15-x Materials. Int. J. Adhes. Adhes. 2022, 112, No. 103024.
(33) Cunha, A.; Elie, A.-M.; Plawinski, L.; Serro, A. P.; Botelho do Rego, A. M.; Almeida, A.; Urdaci, M. C.; Durrieu, M.-C.; Vilar, R. Femtosecond Laser Surface Texturing of Titanium as a Method to Reduce the Adhesion of Staphylococcus aureus and Biofilm Formation. Appl. Surf. Sci. 2016, 360, 485−493.
(34) Azeredo, J.; Visser, J.; Oliveira, R. Exopolymers in Bacterial Adhesion: Interpretation in terms of DLVO and XDLVO Theories. Colloids Surf., B 1999, 14, 141−148.
(35) Du, C.; Wang, C.; Sui, J.; Zheng, L. Enhancing Staphylococcus aureus Sterilization of Stainless Steel by the Synergistic Effect of Surface Structure and Physical Washing. Colloids Surf., B 2021, 197, No. 111393.
(36) Du, C.; Wang, C.; Zhang, T.; Zheng, L. Antibacterial Performance of Zr-BMG, Stainless Steel, and Titanium Alloy with Laser-Induced Periodic Surface Structures. ACS Appl. Bio Mater. 2022, 5, 272−284.
(37) Lorenzetti, M.; Dogsa, I.; Stosicki, T.; Stopar, D.; Kalin, M.; Kobe, S.; Novak, S. The Influence of Surface Modification on Bacterial Adhesion to Titanium-Based Substrates. ACS Appl. Mater. Interfaces 2015, 7, 1644−1651.
(38) Dissanayake, D.; Achola, L. A.; Kerns, P.; Rathnayake, D.; He, J.; Macharia, J.; Suib, S. L. Aerobic Oxidative Coupling of Amines to Imines by Mesoporous Copper Aluminum Mixed Metal Oxides via Generation of Reactive Oxygen Species (ROS). Appl. Catal., B 2019, 249, 32−41.
(39) Sun, J.; Fan, Y.; Ye, W.; Tian, L.; Niu, S.; Ming, W.; Zhao, J.; Ren, L. Near-Infrared Light Triggered Photodynamic and Nitric Oxide Synergistic Antibacterial Nanocomposite Membrane. Chem. Eng. J. 2021, 417, No. 128049.
(40) Nkou Bouala, G. I.; Etiemble, A.; Der Loughian, C.; Langlois, C.; Pierson, J. F.; Steyer, P. Silver Influence on the Antibacterial Activity of Multi-Functional Zr-Cu Based Thin Film Metallic Glasses. Surf. Coat. Technol. 2018, 343, 108−114.
(41) Caicedo, M.; Jacobs, J. J.; Reddy, A.; Hallab, N. J. Analysis of Metal Ion-Induced DNA Damage, Apoptosis, and Necrosis in Human (Jurkat) T-cells Demonstrates Ni2+ and V3+ are more Toxic than other Metals: Al3+, Be2+, Co2+, Cr3+, Cu2+, Fe3+, Mo5+, Nb5+, Zr2+. J. Biomed. Mater. Res., Part A 2008, 86A, 905−913.
(42) De Matteis, V.; Malvindi, M. A.; Galeone, A.; Brunetti, V.; De Luca, E.; Kote, S.; Kshirsagar, P.; Sabella, S.; Bardi, G.; Pompa, P. P. Negligible Particle-Specific Toxicity Mechanism of Silver Nano- particles: the Role of Ag+ Ion Release in the Cytosol. Nanomedicine 2015, 11, 731−739.